

Highly Active and Durable Air Electrodes for Reversible Protonic Ceramic Electrochemical Cells Enabled by An Efficient Bifunctional Catalyst

Yinghua Niu[†], Yucun Zhou[†], Weilin Zhang, Yanxiang Zhang, Conor Evans, Zheyu Luo, Nicholas Kane, Yong Ding, Yu Chen, Xuyun Guo, Weiqiang Lv^{*}, Meilin Liu^{*}

Dr. Yinghua Niu, Dr. Yucun Zhou, Weilin Zhang, Conor Evans, Zheyu Luo, Nicholas Kane, Dr. Yong Ding, Prof. Meilin Liu

School of Materials Science and Engineering, Georgia Institute of Technology, Atlanta, GA 30332-0245, USA.

Email: meilin.liu@mse.gatech.edu

Dr. Yinghua Niu, Dr. Weiqiang Lv

Yangtze Delta Region Institute (Huzhou) & School of Physics, University of Electronic Science and Technology of China, Huzhou, 313001, China.

Email: eselwq@uestc.edu.cn

Dr. Yanxiang Zhang

National Key Laboratory for Precision Hot Processing of Metals, MIIT Key Laboratory of Advanced Structure-Function Integrated Materials and Green Manufacturing Technology, School of Materials Science and Engineering, Harbin Institute of Technology, Harbin, 150001, China.

Prof. Yu Chen

School of Environment and Energy, South China University of Technology, Guangzhou 510006, China.

This is the author manuscript accepted for publication and has undergone full peer review but has not been through the copyediting, typesetting, pagination and proofreading process, which may lead to differences between this version and the [Version of Record](#). Please cite this article as [doi: 10.1002/aenm.202103783](https://doi.org/10.1002/aenm.202103783).

This article is protected by copyright. All rights reserved.

Dr. Xuyun Guo

Department of Applied Physics, Research Institute for Smart Energy, The Hong Kong Polytechnic University, Hung Hom, Kowloon, Hong Kong, China.

† YH Niu and YC Zhou contributed equally to this work.

Keywords: solid oxide cells, air electrode, bifunctional catalyst, water electrolysis, protonic ceramic electrochemical cells

The commercialization of reversible protonic ceramic electrochemical cells (R-PCECs) is hindered by the lack of highly active and durable air electrodes exposed to high concentration of steam under operating conditions. Here we report our findings in dramatically enhancing the electro-catalytic activity and stability of a conventional $(\text{La}_{0.6}\text{Sr}_{0.4})_{0.95}\text{Co}_{0.2}\text{Fe}_{0.8}\text{O}_{3-\delta}$ (LSCF) air electrode by a multiphase catalyst coating composed of a conformal $\text{Pr}_{1-x}\text{Ba}_x\text{CoO}_{3-\delta}$ thin film and exsolved $\text{BaCoO}_{3-\delta}$ nanoparticles. At 600 °C, the catalyst coating decreases the polarization resistance of the LSCF air electrode by a factor of 25 (from 1.09 to 0.043 $\Omega \text{ cm}^2$) in air and the degradation rate by two orders of magnitude (from 1.0×10^{-2} to $1.8 \times 10^{-4} \Omega \text{ cm}^2 \text{ h}^{-1}$ in humidified air with 30 v.% H_2O). Further, a single cell with the catalyst-coated LSCF air electrode at 600 °C demonstrates a high peak power density of 1.04 W cm^{-2} in the fuel cell mode and a high current density of 1.82 A cm^{-2} at 1.3 V in the electrolysis mode. The significantly enhanced performance of the LSCF air electrode is attributed mainly to the high rate of surface oxygen exchange, fast surface proton diffusion, and the rapid H_2O and O_2 dissociation on the catalysts.

This article is protected by copyright. All rights reserved.

1. Introduction

Solid oxide cells (SOCs) are considered efficient and clean energy conversion and storage technologies because of their excellent flexibility in reversible operation on the modes of fuel cells (FCs) and electrolytic cells (ECs).^[1-3] A central goal of current research on SOCs is to reduce the working temperatures to intermediate-to-low temperatures (500~700 °C) for the purpose of improving thermal cycling tolerance, facilitating dynamic response, and reducing the system costs.^[4-6] In particular, the reversible protonic ceramic electrochemical cells (R-PCECs) operated at reduced temperatures have attracted much attention in recent years because of their excellent performance (due to the low activation energies for proton transport) as well as the production of pure and dry H₂ in the electrolysis mode.^[7-10]

To make R-PCECs commercially competitive at intermediate-to-low temperatures, one of the main priorities is to develop air electrodes with high electrocatalytic activity and stability.^[8,11,12] However, the kinetics of oxygen evolution reaction (OER) and oxygen reduction reaction (ORR) at the air electrode decreases exponentially as the working temperature is reduced, significantly increasing the polarization resistance (R_p) of the R-PCECs.^[6,13,14] In addition, at the air electrode of a R-PCEC, a large amount of water is generated in the fuel cell mode and consumed in the electrolysis mode, further exacerbating the polarization losses and poor stability of the air electrode. Since water is generated and consumed at the fuel electrode, not the air electrode, of the SOCs based on an oxygen ion conducting electrolyte (O-SOCs),^[15] most air electrodes designed for O-SOCs may not be suitable for R-PCECs due to the insufficient catalytic activity and stability in high concentration of water at low temperatures.^[16] For instance, air electrode materials

This article is protected by copyright. All rights reserved.

$\text{Ba}_{0.5}\text{Sr}_{0.5}\text{Co}_{0.8}\text{Fe}_{0.2}\text{O}_{3-\delta}$ (BSCF) and $\text{PrBa}_{0.5}\text{Sr}_{0.5}\text{Co}_{2-x}\text{Fe}_x\text{O}_{5+\delta}$ (PBSCF) show high catalytic activity at low temperatures but suffer from significant degradation in high-concentration water.^[17,18] The commercialized $\text{La}_{0.6}\text{Sr}_{0.4}\text{Co}_{0.2}\text{Fe}_{0.8}\text{O}_{3-\delta}$ (LSCF) is one of the widely used air electrodes for O-SOCs.^[19,20] However, LSCF air electrodes exhibit large polarization resistance at low temperatures due to the sluggish ORR/OER kinetics and poor stability caused by surface Sr segregation.^[21-24] Rational design of catalyst-coated LSCF through solution infiltration is an efficient approach to developing air electrodes with tuneable surface chemistry and nanostructures that enhance the electro-catalytic activity at reduced temperatures,^[20,25-27] and to improve the stability in humid air through suppressing surface Sr segregation.^[14,28,29]

The morphology of the catalyst coating is of great importance to the performance and stability of air electrodes.^[19] The coating composed of nanoparticles can effectively enhance the electrode activity, but may not be able to fully stabilize the electrode due to insufficient surface coverage. A conformal coating can protect the air electrode from degradation, yet may sacrifice the catalytic activity due to the reduced specific surface areas for ORR/OER.^[20,30] Taking both catalytic activity and stability into consideration, the catalyst coating composed of a conformal film decorated by nanoparticles may be the best option.^[14,25,28]

Compared with other air electrode materials (e.g., $\text{La}_2\text{NiO}_{4+\delta}$, BSCF, $\text{La}_2\text{CoO}_{4+\delta}$, and $\text{GdBaCo}_2\text{O}_{6-\delta}$), $\text{PrBaCo}_2\text{O}_{6-\delta}$ shows higher mixed ionic and electronic conductivities as well as faster oxygen ion diffusion and surface exchange kinetics at low temperatures.^[31-33] However, the high cost of praseodymium and cobalt as well as the mismatch in thermal expansion coefficient with other cell components limit its practical applications.^[32,34,35] Thus, $\text{PrBaCo}_2\text{O}_{6-\delta}$ is suggested to be used as a thin-film catalyst coating for the air electrode rather

This article is protected by copyright. All rights reserved.

than the electrode backbone. Recently, we developed a $\text{BaCoO}_{3-\delta}$ (BCO) nanoparticle coating on LSCF to enhanced the ORR/OER activity and durability of the air electrode for both oxygen ion-conducting fuel cells and R-PCECs.^[29,36] Despite the excellent activity, degradation of the catalyst-coated electrode was still observed, due likely to insufficient protection of the LSCF electrode since the BCO nanoparticles were not able to form a conformal coating to cover the whole LSCF surface.^[19]

In this work, a new multi-phase (MP) catalyst coating, composed of a conformal $\text{Pr}_{1-x}\text{Ba}_x\text{CoO}_{3-\delta}$ (PBC) thin film and *in situ* exsolved BCO nanoparticles, has been developed for LSCF air electrodes of R-PCECs by infiltration (**Figure 1**). The MP catalyst coating significantly enhanced the catalytic activity and stability of the LSCF air electrode in a high concentration of water. The catalyst-coated LSCF air electrode showed a minimal polarization resistance of $0.043 \Omega \text{ cm}^2$ at $600 \text{ }^\circ\text{C}$, which is only 1/25 of that for the bare LSCF when tested under the same conditions. The catalyst coating reduced the degradation rate of the LSCF air electrode by two orders of magnitude, i.e., from 1.0×10^{-2} to $1.8 \times 10^{-4} \Omega \text{ cm}^2 \text{ h}^{-1}$ at $600 \text{ }^\circ\text{C}$ and 30 v.% H_2O . The MP catalyst-coated LSCF air electrodes were further applied to R-PCECs with $\text{BaZr}_{0.1}\text{Ce}_{0.7}\text{Y}_{0.1}\text{Yb}_{0.1}\text{O}_{3-\delta}$ (BZCYYb) electrolyte, exhibiting superior performance. In addition, a density functional theory (DFT) study was performed to understand the ORR/OER kinetics and stability of the MP catalyst-coated LSCF electrodes.

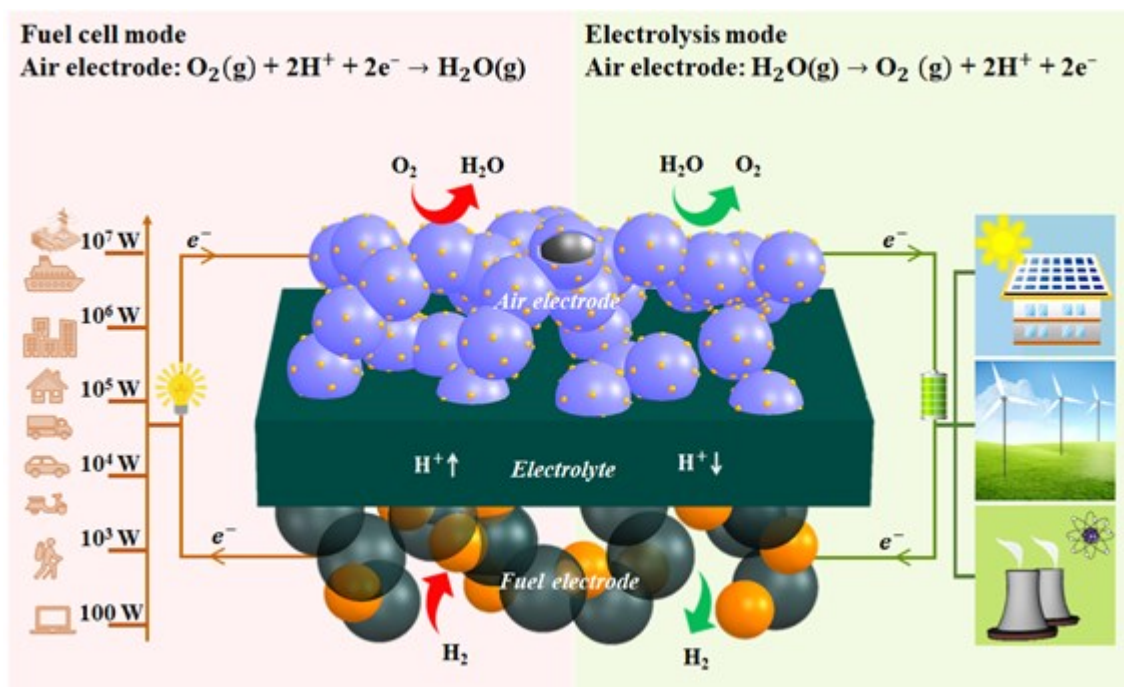


Figure 1. Schematic illustration of a reversible protonic ceramic electrochemical cell with a multi-phase catalyst-coated air electrode.

2. Results and discussion

The morphology and structure of the catalyst-coated LSCF electrodes were revealed by scanning electron microscope (SEM) and transmission electron microscopy (TEM) images.

Figure 2a is a typical SEM image showing the catalyst-coated LSCF air electrode with nanoparticles on the surface. The morphology of the coating is tuneable by changing the catalyst loading and the best loading was ~ 7.5 wt.% of the LSCF backbone (**Figure S1** and

Figure S2). The electron energy-loss spectroscopy (EELS) spectra mapping was conducted (**Figure 2b** and **Figure 2c**) to gain better insight into the composition of the catalyst coating.

The EELS results show that there is no Pr in the outermost nanoparticles, which is most likely composed of $\text{BaCoO}_{3-\delta}$, and the layer on LSCF contains Ba, Co, and Pr, which is more likely belong to $\text{Pr}_{1-x}\text{Ba}_x\text{CoO}_{3-\delta}$. The phases of BCO nanoparticles and the PBC film are

This article is protected by copyright. All rights reserved.

confirmed by the X-ray diffraction (XRD) measurements (**Figure S3**). The high-resolution TEM (HR-TEM) image further provides the evidence for the existence and distribution of the PBC phase. The existence of $(020)_p$ plane in **Figure 2d** indicates the formation of double perovskite PBC, where the subscript p represents the simple perovskite unit cell. The fast Fourier transform (FFT) are applied to the framed areas (i) and (ii) of **Figure 2e** along the $[001]_p$ zone axis. The FFT patterns in **Figure 2e(i)** are from the surface of LSCF away from the edge of the LSCF grain, while those in **Figure 2e(ii)** from the outmost surface of LSCF. The superlattice diffraction spots at position of $1/2 \{010\}$ as directed by the arrow can be found in both **Figure 2e(i)** and **Figure 2e(ii)**. The superlattice diffraction spots may come from the conformal coating layer of PBC, since no superlattice diffraction spots could be observed at $1/2 \{010\}$ in LSCF.^[25,28] Further, the FFT patterns in **Figure 2e(ii)** confirms the epitaxial thin film of PBC grows on the LSCF surface and form a core shell structure as illustrated in **Figure 1**, which is most likely due to the similar structures between PBC and LSCF (**Figure 2f** and **Figure S3**). The EELS spectra in **Figure 2g** shows that Pr, Ba, and Co are found on the surface of the LSCF particle, indicating the formation of double perovskite PBC, which is consistent with the above results.

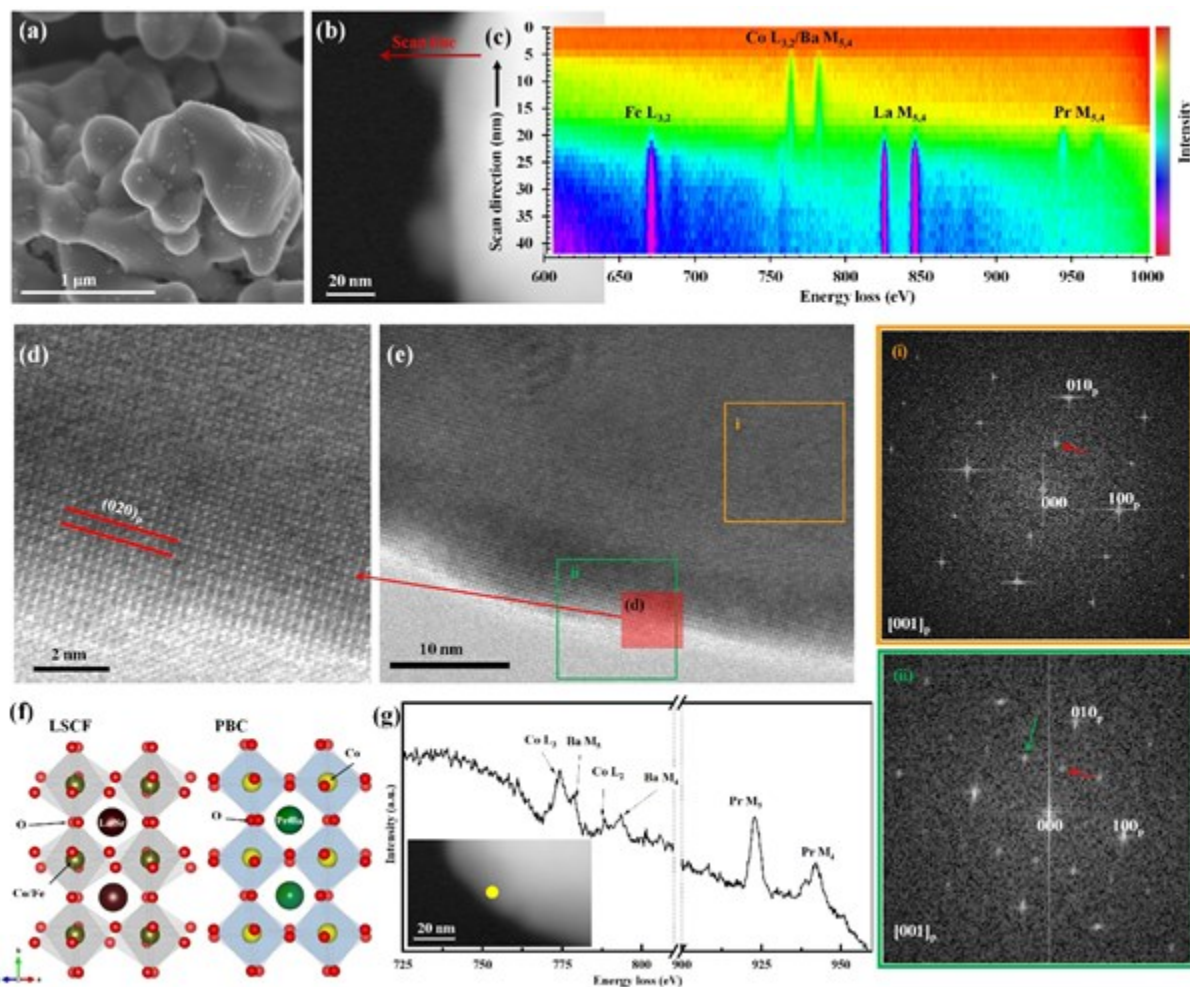


Figure 2. a) The SEM image of the catalyst (~7.5 wt.%) coated LSCF air electrode. b) The high-angle annular dark-field (HAADF) STEM image of the catalyst-coated LSCF with the marked scan line for EELS. c) EELS spectra referring to the scan line in (b) shows Fe L_{3,2}, Co L_{3,2}, Ba M_{5,4}, La M_{5,4}, and Pr M_{5,4} edges. d) The HR-TEM image of the catalyst-coated LSCF with conformal coating layer in the edge select from the colored areas in (e). e) The HR-TEM image, and the FFT patterns of the framed area (i) and (ii) view along the [001]_p axis. f) Unit-cell polyhedral structure of both PBC and LSCF showing an orthorhombic phase. g) EELS spectra referring to the yellow point of the inset HAADF STEM image.

The MP-catalyst dramatically enhanced the catalytic activity of the bare LSCF air electrode. As shown in **Figure 3a**, the R_p of the catalyst-coated LSCF air electrode are very low: 0.016, 0.026, 0.043, and 0.074 $\Omega \text{ cm}^2$ at 700, 650, 600, and 550 $^\circ\text{C}$, respectively. A comparison of the R_p values for the bare and the catalyst-coated LSCF air electrodes at 500-750 $^\circ\text{C}$ are summarized in **Figure 3b**. Clearly, the R_p values of the catalyst-coated LSCF air electrode are significantly smaller than those of the bare electrodes. For instance, the R_p of the catalyst-coated LSCF is 0.074 $\Omega \text{ cm}^2$ at 550 $^\circ\text{C}$, which is about two orders of magnitude lower than that of the bare LSCF air electrode (3.99 $\Omega \text{ cm}^2$) measured under the same conditions. It is noted that these R_p values of the catalyst-coated LSCF air electrodes are even smaller than those of the $\text{BaCo}_{0.4}\text{Fe}_{0.4}\text{Zr}_{0.1}\text{Y}_{0.1}\text{O}_{3-\delta}$ (BCFZY)^[37] and $\text{PrBa}_{0.8}\text{Ca}_{0.2}\text{Co}_2\text{O}_{5+\delta}$ (PBCC),^[38] which have been reported as promising air electrodes for R-PCECs.^[9,11] In addition, Arrhenius plots in **Figure 3b** indicate that the activation energy (E_a) of the catalyst-coated LSCF (0.75 eV) is substantially smaller than that of the bare LSCF (1.35 eV), and is lower than those of other reported air electrodes, including BSCF (1.20 eV),^[39] BCFZY (0.82 eV),^[37] PBCC (1.13 eV),^[38] $\text{Sr}_{0.9}\text{Ce}_{0.1}\text{Fe}_{0.8}\text{Ni}_{0.2}\text{O}_{3-\delta}$ (SCFN, 1.58 eV)^[40] and other catalyst-coated LSCF electrodes (**Figure S4**). Such a low E_a of the MP catalyst-coated LSCF air electrode implies that there is a great potential for low-temperature operation.

Electrical conductivity relaxation (ECR) measurements were adopted to assess the surface exchange coefficient (k^*) of the catalyst-coated air electrodes (**Figure S5**). As shown in **Figure 3c**, the k^* value of the catalyst-coated LSCF ($9.30 \times 10^{-4} \text{ cm s}^{-1}$) is about two orders of magnitude larger than that of the bare LSCF ($1.29 \times 10^{-5} \text{ cm s}^{-1}$) at 650 $^\circ\text{C}$, indicating that the enhanced catalytic activity of the MP catalyst-coated LSCF air electrode is attributed mainly to the accelerated kinetics of the surface oxygen exchange process. The activation

energy of the surface oxygen exchange (E_{a,k^*}) for the catalyst-coated LSCF is 0.81 eV. This is much smaller than that for the bare LSCF ($E_{a,k^*} = 1.84$ eV) (**Figure 3c**). The result of the reduced E_{a,k^*} by the catalyst coating from the ECR measurements is consistent with the polarization results shown in **Figure 3b**. The activation energy of E_{a,k^*} for the MP catalyst-coated LSCF is smaller than the reported values for $\text{PrBa}_{1-x}\text{Co}_2\text{O}_{5+\delta}$ (PBC, $x = 0\sim 0.1$) ($E_{a,k^*} = 0.94\sim 1.18$ eV),^[41] and comparable with the newly developed $\text{BaCo}_{0.7}(\text{Ce}_{0.8}\text{Y}_{0.2})_{0.3}\text{O}_{3-\delta}$ (BCCY) ($E_{a,k^*} = 0.81$ eV) air electrodes.^[42]

Evolution of the higher/lower-frequency arcs with temperature is observed in the electrochemical impedance spectra (EIS) of the catalyst-coated LSCF air electrode (**Figure 3a**). To get better understanding of the kinetics of the electrode reactions, relaxation time distribution (DRT) analysis of EIS data was used. **Figure 3d** shows the DRT plots for the bare and catalyst-coated LSCF electrodes measured at 600 °C in air. The DRT plots can be divided into the peaks distributed in low frequency (LF, <10 Hz), intermediate frequency (IF, 10~2000 Hz), and high frequency (HF, >2000 Hz), which are normally associated with the gas diffusion process, surface oxygen exchange process, and charge transfer process, respectively.^[26,43] The catalyst-coated LSCF electrode shows a substantially smaller IF peak than the bare LSCF (**Figure 3d**), indicating a dramatically enhanced surface oxygen exchange process (including oxygen surface adsorption/desorption, dissociation, and transport).^[26] This is consistent with the ECR measurement shown in **Figure 3c**. EIS of the air electrodes measured under different partial pressure of O_2 (p_{O_2}) were further analyzed (**Figure S6** and **Figure 3e**). Total R_p was separated into R_{LF} , R_{IF} , and R_{HF} , representing the R_p of the LF, IF, and HF ranges, respectively. The relationship between R_p and p_{O_2} can be expressed by the equation of $R_i = kp_{\text{O}_2}^{-n}$, where k is a constant, the exponent n indicates the reaction order respect to p_{O_2} .^[36,38] As shown in **Figure 3f**, the n values for the R_{LF} , R_{IF} , and R_{HF} are 1.29, 0.82, and 0.13, respectively, indicating that the LF arc corresponds to

the mass transport process, the IF arc to the surface oxygen exchange process, and the HF arc to the charge transfer process.

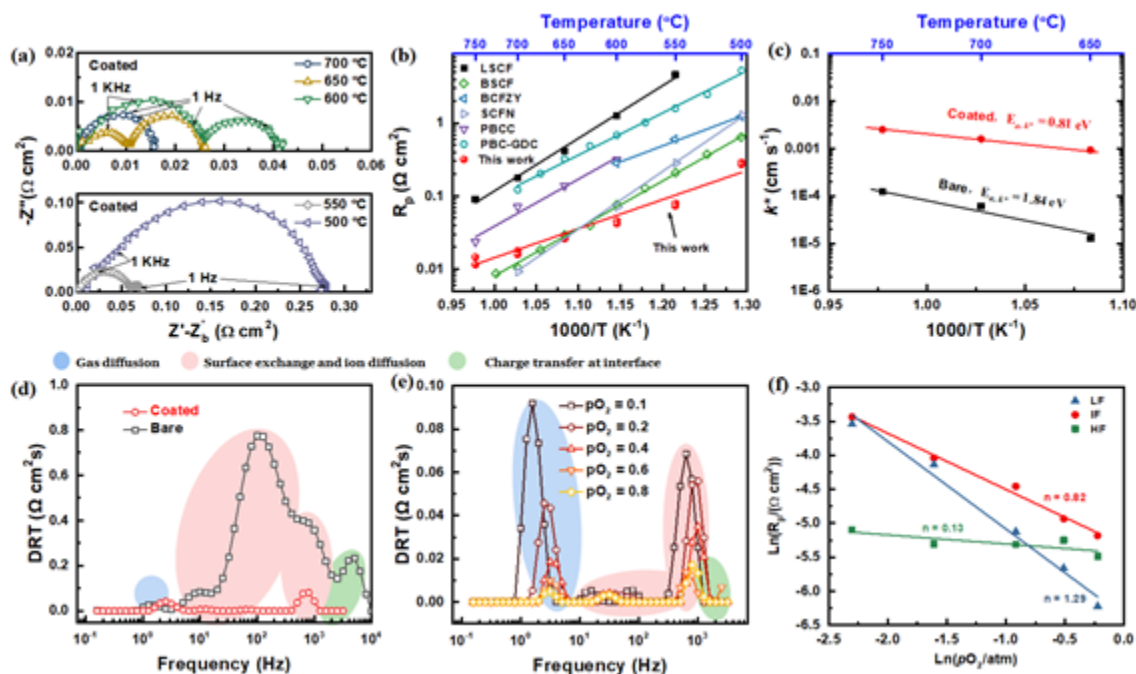


Figure 3. a) EIS of $\text{Ce}_{0.8}\text{Sm}_{0.2}\text{O}_{2-\delta}$ (SDC)-based symmetrical cells using catalyst (~ 7.5 wt.%) coated LSCF as the air electrode measured at 700-500 °C in air. b) Temperature dependence of polarization resistances of the LSCF air electrodes before and after catalyst coating. The R_p values of BSCF,^[39] BCFZY,^[37] SCFN,^[40] PBCC^[38] and PBC-SDC^[44] electrodes from literatures are included for comparison. c) Temperature dependence of k^* of the bare LSCF and catalyst-coated LSCF bars at 650-750 °C. d) DRT analysis of the EIS data of the LSCF air electrodes with and without catalyst coating measured at 600 °C in air. e) DRT studies of the EIS of catalyst-coated LSCF measured under different p_{O_2} at 600 °C. f) R_p respond to the change of p_{O_2} of the catalyst-coated LSCF air electrode at 600 °C.

The MP-catalyst coating effectively enhanced the stability of the LSCF air electrode in both ambient air and humid air (Figure S7, Figure S8, and Figure 4a). For example, as shown in Figure

4a, the degradation rate of the catalyst-coated LSCF ($8.1 \times 10^{-5} \Omega \text{ cm}^2 \text{ h}^{-1}$) is neglectable after a 408 h-test under open circuit voltage (OCV) conditions when compared with that of the bare LSCF electrode ($2.2 \times 10^{-3} \Omega \text{ cm}^2 \text{ h}^{-1}$). The enhanced stability of the catalyst-coated LSCF was also observed under a high concentration of steam. As shown in **Figure 4b**, the degradation rate of the catalyst-coated LSCF air electrodes under OCV in 30 v.% H₂O is $1.8 \times 10^{-4} \Omega \text{ cm}^2 \text{ h}^{-1}$, nearly two orders of magnitude lower than that of the bare LSCF air electrodes ($1.0 \times 10^{-2} \Omega \text{ cm}^2 \text{ h}^{-1}$). No obvious change in electrode morphology is observed after the long-term stability test in air with 30 v.% and 50 v.% H₂O (**Figure S7**), further confirming the excellent stability of the catalyst-coated LSCF air electrode under the operation conditions. To mimic the reversible operation of single cells, a cyclic bias of $\pm 1.5 \text{ V}$ with a duration of 11.5 h for each cycle was applied to the symmetrical cells immersed in humidified air with 30 v.% H₂O. The degradation rate of the catalyst-coated LSCF electrodes under the cycling mode is $1.6 \times 10^{-4} \Omega \text{ cm}^2 \text{ h}^{-1}$ (**Figure 4b**). This is comparable to the degradation rate under the static mode, thus demonstrating excellent reversibility under dynamic cycling conditions. **Figure 4c** shows the stable operation of the catalyst-coated electrode under the reversible operation mode for over 8 cycles. In contrast, a significant current drop was observed for the cells with bare LSCF air electrodes operated under the same cycling conditions. By analyzing the evolution of EIS of the bare LSCF electrode with testing time, it is found that the degradation is due mainly to the increased IF peak (**Figure 4d**), indicating the deteriorated surface reaction activity. For the catalyst-coated LSCF air electrode, the increase in the IF peak is insignificant (**Figure 4e**). It implies that the catalyst coating stabilized the LSCF electrode by inhibiting the deterioration of the catalytic kinetics, most likely through suppression of Sr segregation.^[36,45] Similarly, the enhanced activity and stability of the catalyst-coated LSCF air electrode was also observed in BZCYYb electrolyte-based symmetrical cells (**Figure S9**).

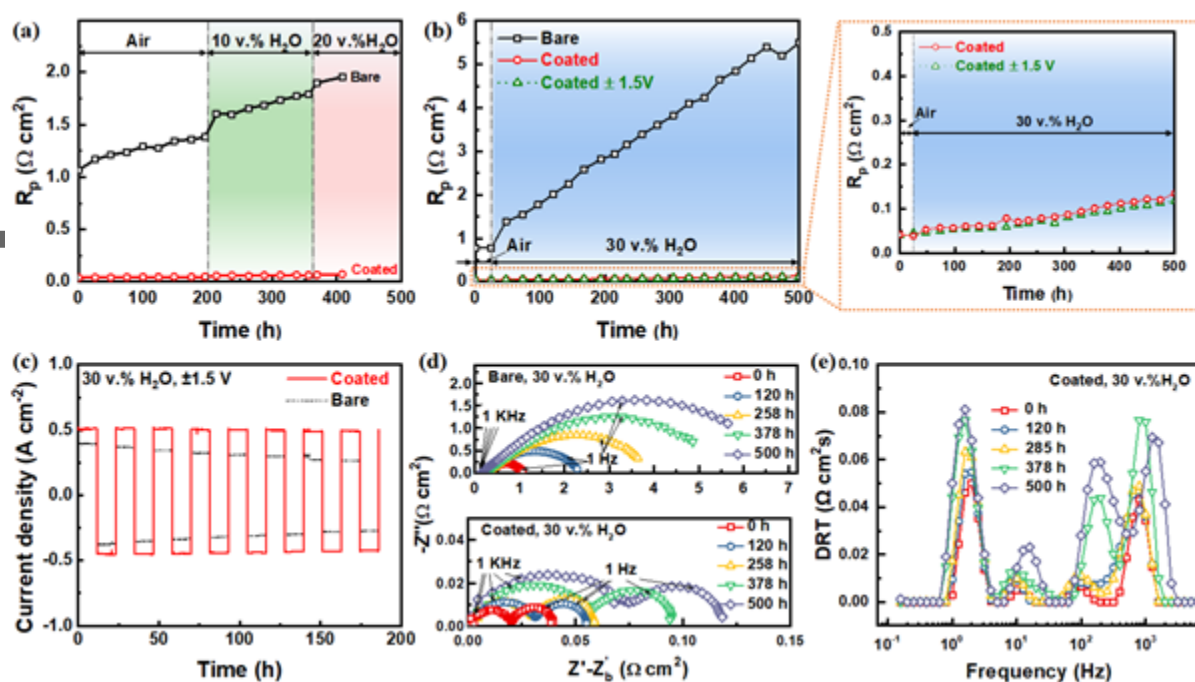


Figure 4. Long-term stability tests of SDC-based symmetrical cells with bare and catalyst (~7.5 wt.%) coated LSCF air electrodes at 600 °C. a) In air for the initial 200 h, followed by in 10 v.% -H₂O air for 162 h, and then in 20 v.% H₂O-air for 46 h under OCV conditions. b) Stability test in air for the initial 24 h, followed by in 30 v.% H₂O-air for 475 h. The bare LSCF cell was tested under OCV, one of the catalyst-coated LSCF cell was tested under OCV, and another catalyst-coated cell was tested under the cyclic bias of ±1.5 V with 11.5 h for each cycle. c) The plots of measured cell current density *versus* time for the bare and catalyst-coated LSCF cells tested under the cyclic bias of ±1.5 V in 30 v.% H₂O air. d) EIS of the bare and catalyst-coated LSCF cells measured at different time under OCV conditions in 30 v.% H₂O air. e) DRT analysis of the EIS of the catalyst-coated LSCF electrode measured at different time under OCV in 30 v.% H₂O air.

The highly active and stable catalyst-coated LSCF air electrode was further applied to R-PCECs. As shown in the cross-sectional SEM images in **Figure 5a-c**, the single cell is composed of a Ni-BZCYYb fuel electrode, a BZCYYb electrolyte ($\approx 10 \mu\text{m}$ thickness), and a catalyst-coated LSCF air electrode. When operated in the fuel cell mode in wet H_2 (3 v.% H_2O) and air, the single cell with a catalyst-coated LSCF air electrode shows high maximum power densities (P_{max}) of 1.67, 1.04, 0.62, and 0.39 W cm^{-2} at 650, 600, 550 and $500 \text{ }^\circ\text{C}$, respectively. Compared with the cell using a bare LSCF electrode, the cell with catalyst-coated LSCF achieved ≈ 1.6 times higher power output at temperatures of $550\text{--}650 \text{ }^\circ\text{C}$ (**Figure 5e** and **Figure S10**). The comparison of P_{max} of proton-conducting electrolyte-based SOFCs with LSCF-based air electrodes is provided in **Figure 5f**. The P_{max} achieved in this work is the highest ever reported, demonstrating the high activity of the catalyst-coated LSCF air electrode. By comparing the EIS of the single cells (**Figure S11**), it is found that the improvement in cell performance by the catalyst coating is attributed to the decreased polarization resistance, most likely due to the enhanced catalytic activity of the air electrode. When operated in the water electrolysis mode, the enhanced performance of the cell with catalyst-coated LSCF electrode was also observed (**Figure S12** and **Figure 5g, h**). For example, at a cell voltage of 1.3 V, the catalyst-coated cell (**Figure S12a**) showed high current densities of 3.13, 1.82, and 0.85 A cm^{-2} at 650, 600, and $550 \text{ }^\circ\text{C}$, which is about 1.79, 1.54 and 1.41 times higher than the current densities achieved in the cell without catalyst coating (**Figure 5h**), respectively. The excellent durability of the catalyst-coated LSCF air electrode was further verified by testing single cells in the electrolysis mode for over 300 h in wet air with 3 v.% H_2O (**Figure 5i**) and over 100 h in humidified air with 50 v.% H_2O (**Figure S13**).

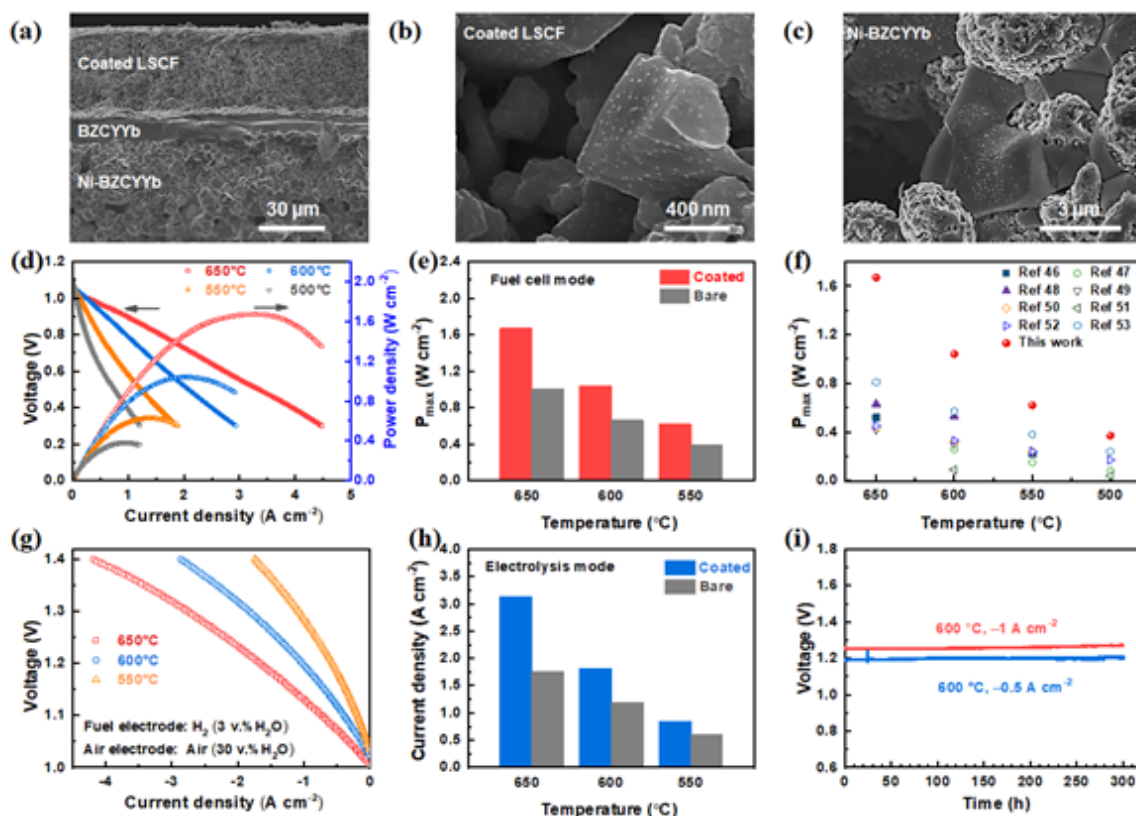


Figure 5. Morphology and performance of the catalyst-coated single cells. SEM images of a) Ni-BZCYYb/BZCYYb/catalyst-coated LSCF single cell, b) the catalyst-coated LSCF air electrode, c) the Ni-BZCYYb fuel electrode. d) Typical current-voltage-power density (I-V-P) curves measured in the FC mode at 500-650 °C supplying with humid hydrogen (97 v.% H₂ + 3 v.% H₂O) and air to the fuel electrode and air electrode, respectively; e) Comparison of P_{\max} of single cells with LSCF air electrodes with and without catalyst coating; f) Temperature dependence of P_{\max} . P_{\max} of protonic ceramic electrochemical cells using LSCF-based air electrodes reproduced from Ref. [46], Ref. [47], Ref. [48], Ref. [49], Ref. [50], Ref. [51], Ref.[52] and Ref. [53] are added for comparison; g) The current-voltage (I-V) characteristics in the EC mode at 500-650 °C with H₂ (3 v.% H₂O) and air (30 v.% H₂O) in the fuel and air electrodes, respectively; h) Comparison of electrolysis current densities between two types of single cells at 1.3 V; i) Durability tests in the electrolysis mode at current densities of -0.5 A cm^{-2} and -1 A cm^{-2} with H₂ (3 v.% H₂O)/air (3% H₂O).

DFT calculations are a powerful tool for revealing the molecular/atomic level mechanisms of electrode processes. For example, the electro-catalytic processes on BCO nanoparticles have been investigated in previous studies,^[26,36,54] suggesting that the surface diffusion of dissociated oxygen species is sufficiently fast on BCO nanoparticles. In this work, we performed DFT calculations to gain insight into the reversible ORR/OER on PBC surfaces. **Figure 6** shows the energy profile for the OER from the left to right and the ORR from the right to the left on PrCoO-terminated (110) surface since its surface energy is slightly lower than that of the BaCoO-terminated (110) surface (**Figure S14-S15**). In the electrolysis mode, the OER process includes the following steps: H₂O adsorption, the dissociation of H₂O to *OH and to *H (the symbol * means that the species are adsorbed on the surface), the dissociation of *OH to *H and *O, the combination of two *O to *O₂, and the desorption of *O₂ from the surface to free O₂ molecule. The adsorption of H₂O and the dissociation of H₂O are spontaneous. In comparison, the dissociation barrier of H₂O on LSCF(001) surface is 0.17 eV.^[36] The barrier for *OH dissociation is 0.58 eV on PBC surface, which is much lower than the barrier energy of 1.19 eV on LSCF(001) surface,^[36] indicating higher activity of the dehydrogenation kinetics of PBC over LSCF. The surface migration barrier for *H is found to be ~0 V, which facilitates the transport of proton from the proton-conducting electrolyte to the air electrode surface and vice versa. The combination of *O to O₂ requires 0.61 eV, but the rate-determining step is the desorption of O₂ from the surface, which has an energy barrier of 1.63 eV. For the ORR process, the rate-determining step is the desorption of H₂O, which has an energy barrier of 1.04 eV. The desorption energy may decrease largely as the coverage of adsorbed species increases, which means the practical OER or ORR barrier should be much lower than the computed values. The energy barrier of ORR on PBC surface (1.04 eV) is lower than that on LSCF(001) surface (1.30 eV).^[36] Overall, the low proton surface diffusion barrier and the low dissociation energy for H₂O and O₂ facilitates largely the OER and ORR kinetics on PBC surfaces. **Figure S16** also provides an alternative OER/ORR mechanism on the surface of Pr_{0.75}Ba_{0.25}CoO₃ with PrCoO-(110) exposed to surface involving *OOH. For the ORR process, the existence of *OOH does not have any impact on the energy barrier and rate-determining

step (the desorption of H_2O). But for the OER process, the dissociation energy of $^*\text{OOH}$ is 2.01 eV, which means that this process is kinetically unfavorable for the OER process.

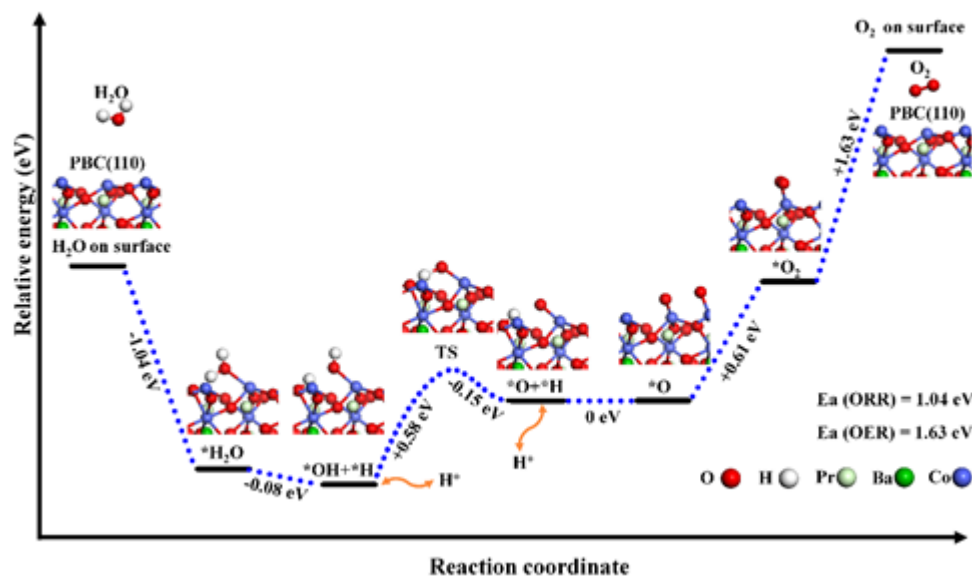


Figure 6. The predicted OER/ORR mechanism on the surface of $\text{Pr}_{0.75}\text{Ba}_{0.25}\text{CoO}_3$. The red, white, blue, and light green balls represent O, H, Co, and Pr atoms, respectively. The OER process including the following steps: H_2O adsorption, dissociation of H_2O to $^*\text{OH}$ to $^*\text{H}$ (where * means that the species are adsorbed on the surface), the dissociation of $^*\text{OH}$ to $^*\text{H}$ and $^*\text{O}$, the combination of two $^*\text{O}$ to $^*\text{O}_2$, and the desorption of $^*\text{O}_2$ from the surface to free O_2 molecule. The ORR process is the reverse process of OER from the right to the left. The energy for each step is marked in black for the OER process and red for the ORR process. The structure of the TS state for $^*\text{OH}$ dissociation is placed nearby. The bottom atomic structures show the configurations of $^*\text{H}_2\text{O}$, $^*\text{H}+^*\text{OH}$, $^*\text{OH}$, $^*\text{O}+^*\text{H}$ and $^*\text{O}_2$, respectively.

3. Conclusion

In summary, both the electrocatalytic activity and stability of the state-of-the-art LSCF air electrode in high humidity have been dramatically enhanced by the application of a conformal PBC thin film coating decorated with exsolved BCO nanoparticles. The high

electrocatalytic activities for ORR and OER as well as the excellent stability of the catalyst-coated LSCF air electrode have been demonstrated in both symmetrical cells and BZCYYb electrolyte-based reversible cells. Electrochemical measurements and DFT calculations indicated that the fast OER and ORR kinetics of the catalyst-coated air electrode was attributed to the fast kinetics of surface oxygen exchange, low proton surface diffusion barrier, and the low dissociation energy for H₂O and O₂. The novel air electrode and the catalyst coating approach are attractive for intermediate-to-low-temperature R-PCECs, and other types of energy conversion and storage systems, including low-temperature O-SOCs and metal-air batteries.

4. Experimental Section

4.1 Preparation of the catalyst solution

The nitrate solutions for surface modification of LSCF electrode via infiltration were prepared by dissolving metal (Me) nitrate precursors, Me(NO₃)_x (or its hydrate), in distilled water with a concentration of 0.1 mol L⁻¹. The raw materials, including Pr(NO₃)₃·6H₂O (99.9%, Alfa-Aesar), Ba(NO₃)₂ (99%, Alfa-Aesar), and Co(NO₃)₂·6H₂O (99%, Sigma-Aldrich) were used as metal sources. Stoichiometric amounts of nitrates for a predetermined target composition of Pr_{0.5}Ba_{0.5}CoO_{3-δ} were dissolved in a mixed solvent (volume ratio of water to ethanol is 4:1). Glycine and polyvinyl pyrrolidone (PVP) were added as a complexing agent and a surfactant, respectively.

4.2 Fabrication of symmetrical cells and single cells

SDC electrolyte-based symmetrical cells instead of the BZCYYb-based cells were used for most investigations of the air electrodes and catalysts since the degradation of BZCYYb in high concentration of steam may affect the evaluation of the stability of air electrodes. The SDC electrolyte-based symmetrical cells with a configuration of LSCF/SDC/LSCF were fabricated as

This article is protected by copyright. All rights reserved.

described in a previous study.^[45] $(\text{La}_{0.6}\text{Sr}_{0.4})_{0.95}\text{Co}_{0.2}\text{Fe}_{0.8}\text{O}_{3-\delta}$ (LSCF-P, SKU: 121205, surface area: $5.8 \text{ m}^2 \text{ g}^{-1}$) powder purchased from FuelCellMaterials Inc. was used as received. $\text{BaZr}_{0.1}\text{Ce}_{0.7}\text{Y}_{0.1}\text{Yb}_{0.1}\text{O}_{3-\delta}$ (BZCYYb) electrolyte-based symmetrical cells with a configuration of LSCF/BZCYYb/LSCF were prepared by screen printing the LSCF ink, composed of LSCF powder (Fuel Cell Materials, US) and terpineol (6 wt.% ethyl cellulose), onto both sides of a dense BZCYYb pellet. The BZCYYb pellets were fabricated by dry pressing grounded BZCYYb powder with 1 wt.% NiO into discs and sintering at $1450 \text{ }^\circ\text{C}$ for 2 h. BZCYYb powder was fabricated by a solid-state reaction process. Stoichiometric amounts of BaCO_3 , ZrO_2 , CeO_2 , Y_2O_3 , and Yb_2O_3 (Aldrich Chemicals) were mixed by ball milling at 400 rpm for 4 h in ethanol, followed by drying and calcining at $1100 \text{ }^\circ\text{C}$ for 12 h in air. The ball milling and calcination process was repeated until the desired electrolyte phase purity was obtained. SDC/BZCYYb electrolyte-based symmetrical cells were co-fired at $1080 \text{ }^\circ\text{C}$ for 2 h to form the porous LSCF backbone with an active area of 0.28 cm^2 . Then, a proper amount (5/10/15/20 μL) of the catalyst precursor solution was infiltrated into the as-prepared LSCF electrodes, followed by firing at $800 \text{ }^\circ\text{C}$ in air for 2 h.

Single cells with the configuration of LSCF|BZCYYb|Ni-BZCYYb were fabricated as described in a previous study.^[36] The anode-supported bi-layer structures (BZCYYb|Ni-BZCYYb) were fabricated by co-tape casting the supporting and function layers of Ni-BZCYYb and a layer of BZCYYb electrolyte. This was followed by co-sintering the green tape in air at $1400 \text{ }^\circ\text{C}$ for 5 h. The single cells were formed by screen printing the LSCF ink onto the electrolyte surface of the bi-layer and then calcining at $1080 \text{ }^\circ\text{C}$ for 2 h. The catalyst was fabricated by infiltrating 15 μL (~7.5 wt.% of the LSCF backbone) precursor solution into the LSCF electrode (active area = 0.28 cm^2) and then firing at $800 \text{ }^\circ\text{C}$ for 2 h in air.

4.3 Electrochemical measurements and DRT calculation

The area specific resistances (ASR) of air electrodes were measured using two pieces of silver mesh as current collectors on both sides of a symmetrical cell from $500 \text{ }^\circ\text{C}$ to $750 \text{ }^\circ\text{C}$ at a temperature interval of $50 \text{ }^\circ\text{C}$. Polarization resistances of the electrodes of the symmetrical cells were determined

This article is protected by copyright. All rights reserved.

from the impedance spectra, the difference in the intercepts with the real axis at low and high frequencies.

Electrochemical impedance spectra were acquired using a Solartron 1255 HF frequency response analyzer coupled with an EG&G Princeton Applied Research (PAR) potentiostat (model 273A) in the frequency range from 1000 kHz to 0.01 Hz. The amplitude of the applied AC voltage is 10 mV. I-V curves of the single cells operated in the FC mode and EC mode were obtained at 500 °C to 650 °C with the fuel electrode and air electrode fed with wet H₂ (3 v.% H₂O) and humidified air (0/3/30/50 v. % H₂O), respectively. The water content in air of inlet at the air electrode was controlled by passing air through a temperature-controlled bubbler. Voltage-time (V-t) curves of the cells were monitored using a multichannel Arbin electrochemical testing system. ECR measurements were recorded using a four-probe DC method at 650 °C to 750°C. The constant current was supplied by a PAR galvanostat and the voltage was recorded using a Keithley meter (Model 2700).

The DRT was calculated using the Tikhonov regularization approach without using a regularization parameter, which was developed in our previous studies.^[55,56] The algorithm treats the “regularization parameter” as an unknown variable varied with frequency, and resolves the distribution of regularization parameter with the DRT at the same time. This algorithm is capable of eliminating the pseudo peaks and capturing discontinuities in the DRT.^[56]

4.4 Characterizations

The morphology of the air electrodes and the cross-sectional views of single cells were characterized using a scanning electron microscope (SEM, Hitachi SU8010). TEM images and bright-field scanning TEM images were acquired using a FEI Tecnai F30 super-twin TEM with super twin objective lens and field-emission-gun operating at an acceleration voltage of 300 kV. A Gatan OneView camera was used to record the HR-TEM images. The EELS spectra were recorded by a Gatan GIF system (Tridiem 863 UHS). The XRD patterns were collected from an X'Pert Alpha-1

This article is protected by copyright. All rights reserved.

diffractometer (Cu K α 1 radiation, $\lambda = 1.5406$).

4.5 Computational method

To gain some insight into the mechanism of the air electrode reactions, DFT calculations were performed. The Cambridge Sequential Total Energy Package (CASTEP) with the ultrasoft plane wave pseudopotential was employed for the calculation under the spin-polarized generalized gradient approximation (GGA) with the Perdew-Burke-Ernzerhof (PBE) exchange-correlation functional. A Pr_{0.75}Ba_{0.25}CoO₃ conventional crystal cell with a space group of *Pnma* was used to simulate the conformal catalyst coating. A kinetic energy cutoff for a plane wave basis set of 420 eV, and Monkhorst-Pack meshes with the (3 × 2 × 3) and (1 × 2 × 1) were used for surface and bulk calculations, respectively. For the surface calculations, the (110) surface models with an atom composition of (Pr_{0.75}Ba_{0.25}CoO₃)₆ were built and the first three layers were allowed for relaxation. Slabs were separated by a vacuum space of 15 Å to avoid any interactions between slabs and the self-consistent dipole correction was applied. The adsorption energy (E_{ad}) of O₂ and H₂O on a surface was calculated by $E_{ad} = E[\text{M-surface}] - (E[\text{surface}] + E[\text{M}])$, where $E[\text{M-surface}]$ and $E[\text{surface}]$ are the predicted electronic energies for an adsorbed species on a surface and its bare surface. $E[\text{M}]$ is the calculated energy of O₂ or H₂O. For the adsorption of other species such as O, H, OH and OOH, the isolated reference states are 1/2O₂, 1/2H₂, H₂O-1/2H₂ and 2H₂O-3/2H₂, respectively. Surface or bulk diffusion barriers of E_m is the migration barrier of an oxygen ion or proton on surface or through bulk phases. E_m was determined by transition state search based on the complete Linear Synchronous Transit (LST)/Quadratic Synchronous Transit (QST) method.

Supporting Information

Supporting Information is available from the Wiley Online Library or from the author.

Acknowledgements

Y.N. and Y.Z. contributed equally to this work. This work was supported by the U.S. Department of Energy, Office of Energy Efficiency and Renewable Energy (EERE) Hydrogen and Fuel Cell R&D Program under the award number DE-EE0008439. This work was also supported by the National Natural Science Foundation of China (Grant. Nos. 52102212 and 51972043) and the Foundation of Yangtze Delta Region Institute (Huzhou) of UESTC, China (Nos. U03210010 and U03210028). Y. Niu acknowledges the financial support of a scholarship from the China Scholarship Council (CSC).

Received: ((will be filled in by the editorial staff))

Revised: ((will be filled in by the editorial staff))

Published online: ((will be filled in by the editorial staff))

References

- [1] W. Wang, D. Medvedev, Z. Shao, *Adv. Fun. Mater.* **2018**, 28, 1802592.
- [2] S. H. Jensen, C. Graves, M. Mogensen, C. Wendel, R. Braun, G. Hughes, Z. Gao, S. A. Barnett, *Energ. Environ. Sci.* **2015**, 8, 2471.
- [3] C. Zhao, Y. Li, W. Zhang, Y. Zheng, X. Lou, B. Yu, J. Chen, Y. Chen, M. Liu, J. Wang, *Energ. Environ. Sci.* **2020**, 13, 53.
- [4] C. Sun, S. Yang, Y. Lu, J. Wen, X. Ye, Z. Wen, *J. Power Sources* **2020**, 449, 227498.
- [5] G. Yang, C. Su, H. Shi, Y. Zhu, Y. Song, W. Zhou, Z. Shao, *Energy & Fuels* **2020**, 34, 15169.
- [6] J. Shin, H. Park, K. Park, M. Saqib, M. Jo, J. H. Kim, H. Lim, M. Kim, J. Kim, J. Park, *J. Mater. Chem. A* **2021**, 9, 607.
- [7] L. Yang, S. Wang, K. Blinn, M. Liu, Z. Liu, Z. Cheng, M. Liu, *Science* **2009**, 326, 126.
- [8] H. Ding, W. Wu, C. Jiang, Y. Ding, W. Bian, B. Hu, P. Singh, C. J. Orme, L. Wang, Y. Zhang, D. Ding, *Nat Commun* **2020**, 11, 1907.
- [9] C. Duan, R. Kee, H. Zhu, N. Sullivan, L. Zhu, L. Bian, D. Jennings, R. O'Hayre, *Nature Energy* **2019**, 4, 230.
- [10] C. Duan, J. Huang, N. Sullivan, R. O'Hayre, *Applied Physics Reviews* **2020**, 7, 011314.
- [11] Y. Zhou, E. Liu, Y. Chen, Y. Liu, L. Zhang, W. Zhang, Z. Luo, N. Kane, B. Zhao, L. Soule, Y. Niu, Y. Ding, H. Ding, D. Ding, M. Liu, *ACS Energy Letters* **2021**, 6, 1511.
- [12] S. Choi, T. C. Davenport, S. M. Haile, *Energ. Environ. Sci.* **2019**, 12, 206.
- [13] Y. Lin, R. Ran, Y. Zheng, Z. Shao, W. Jin, N. Xu, J. Ahn, *J. Power Sources* **2008**, 180, 15.
- [14] Y. Chen, S. Yoo, K. Pei, D. Chen, L. Zhang, B. deGlee, R. Murphy, B. Zhao, Y. Zhang, Y. Chen, M. Liu, *Advanced Functional Materials* **2018**, 28, 1704907.
- [15] J. Kim, A. Jun, O. Gwon, S. Yoo, M. Liu, J. Shin, T.-H. Lim, G. Kim, *Nano Energy* **2018**, 44, 121.
- [16] L. Lei, J. Zhang, Z. Yuan, J. Liu, M. Ni, F. Chen, *Adv. Fun. Mater.* **2019**, 29, 1903805.
- [17] N. Bausá, C. Solís, R. Strandbakke, J. M. Serra, *Solid State Ionics* **2017**, 306, 62.
- [18] M. Choi, S. J. Kim, W. Lee, *Ceramics International* **2021**, 47, 7790.
- [19] M. Liu, M. E. Lynch, K. Blinn, F. M. Alamgir, Y. Choi, *Materials Today* **2011**, 14, 534.
- [20] D. Ding, X. Li, S. Y. Lai, K. Gerdes, M. Liu, *Energy Environ. Sci.* **2014**, 7, 552.
- [21] S. M. Choi, J. Ahn, J. W. Son, J. H. Lee, B. K. Kim, K. J. Yoon, H. I. Ji, *ACS Appl. Mater. Interfaces* **2018**, 10, 39608.

This article is protected by copyright. All rights reserved.

- [22] Y. Yu, K. F. Ludwig, J. C. Woicik, S. Gopalan, U. B. Pal, T. C. Kaspar, S. N. Basu, *ACS Appl. Mater. Interfaces* **2016**, *8*, 26704.
- [23] B. Koo, K. Kim, J. K. Kim, H. Kwon, J. W. Han, W. Jung, *Joule* **2018**, *2*, 1476.
- [24] N. Tsvetkov, Q. Lu, L. Sun, E. J. Crumlin, B. Yildiz, *Nat Mater* **2016**, *15*, 1010.
- [25] Y. Chen, Y. Chen, D. Ding, Y. Ding, Y. Choi, L. Zhang, S. Yoo, D. Chen, B. deGlee, H. Xu, Q. Lu, B. Zhao, G. Vardar, J. Wang, H. Bluhm, E. J. Crumlin, C. Yang, J. Liu, B. Yildiz, M. Liu, *Energy Environ. Sci.* **2017**, *10*, 964.
- [26] Y. Chen, Y. Choi, S. Yoo, Y. Ding, R. Yan, K. Pei, C. Qu, L. Zhang, I. Chang, B. Zhao, Y. Zhang, H. Chen, Y. Chen, C. Yang, B. deGlee, R. Murphy, J. Liu, M. Liu, *Joule* **2018**, *2*, 938.
- [27] K. T. Lee, E. D. Wachsman, *MRS Bulletin* **2014**, *39*, 783.
- [28] Y. Chen, S. Yoo, X. Li, D. Ding, K. Pei, D. Chen, Y. Ding, B. Zhao, R. Murphy, B. deGlee, J. Liu, M. Liu, *Nano Energy* **2018**, *47*, 474.
- [29] K. Pei, Y. Zhou, K. Xu, Z. He, Y. Chen, W. Zhang, S. Yoo, B. Zhao, W. Yuan, M. Liu, Y. Chen, *Nano Energy* **2020**, *72*, 104704.
- [30] T. Yang, Y. Wen, T. Wu, N. Xu, K. Huang, *J. Mater. Chem. A* **2020**, *8*, 82.
- [31] Y. Tian, Y. Liu, W. Wang, L. Jia, J. Pu, B. Chi, J. Li, *J. Energy Chem.* **2020**, *43*, 108.
- [32] G. Kim, S. Wang, A. J. Jacobson, L. Reimus, P. Brodersen, C. A. Mims, *Journal of Materials Chemistry* **2007**, *17*, 2500.
- [33] D. Chen, R. Ran, K. Zhang, J. Wang, Z. Shao, *J. Power Sources* **2009**, *188*, 96.
- [34] J. H. Kim, A. Manthiram, *J. Electrochem. Soc.* **2008**, *155*, B385.
- [35] J. Kim, A. Manthiram, *J. Mater. Chem. A* **2015**, *3*, 24195.
- [36] Y. C. Zhou, W. Zhang, N. Kane, Z. Luo, K. Pei, K. Sasaki, Y. Choi, Y. Chen, D. Ding, M. Liu, *Advanced Functional Materials* **2021**, *31*, 2105386.
- [37] C. Duan, D. Hook, Y. Chen, J. Tong, R. O'Hayre, *Energ. Environ. Sci.* **2017**, *10*, 176.
- [38] Y. Chen, S. Yoo, Y. Choi, J. H. Kim, Y. Ding, K. Pei, R. Murphy, Y. Zhang, B. Zhao, W. Zhang, H. Chen, Y. Chen, W. Yuan, C. Yang, M. Liu, *Energy Environ. Sci.* **2018**, *11*, 2458.
- [39] Z. Shao, S. M. Haile, *Nature* **2004**, *431*, 170.
- [40] Y. Song, Y. Chen, M. Xu, W. Wang, Y. Zhang, G. Yang, R. Ran, W. Zhou, Z. Shao, *Adv Mater* **2020**, *32*, 1906979.
- [41] F. Dong, M. Ni, Y. Chen, D. Chen, M. O. Tadé, Z. Shao, *J. Mater. Chem. A* **2014**, *2*, 20520.
- [42] Y. Song, Y. Chen, W. Wang, C. Zhou, Y. Zhong, G. Yang, W. Zhou, M. Liu, Z. Shao, *Joule* **2019**, *3*, 2842.

This article is protected by copyright. All rights reserved.

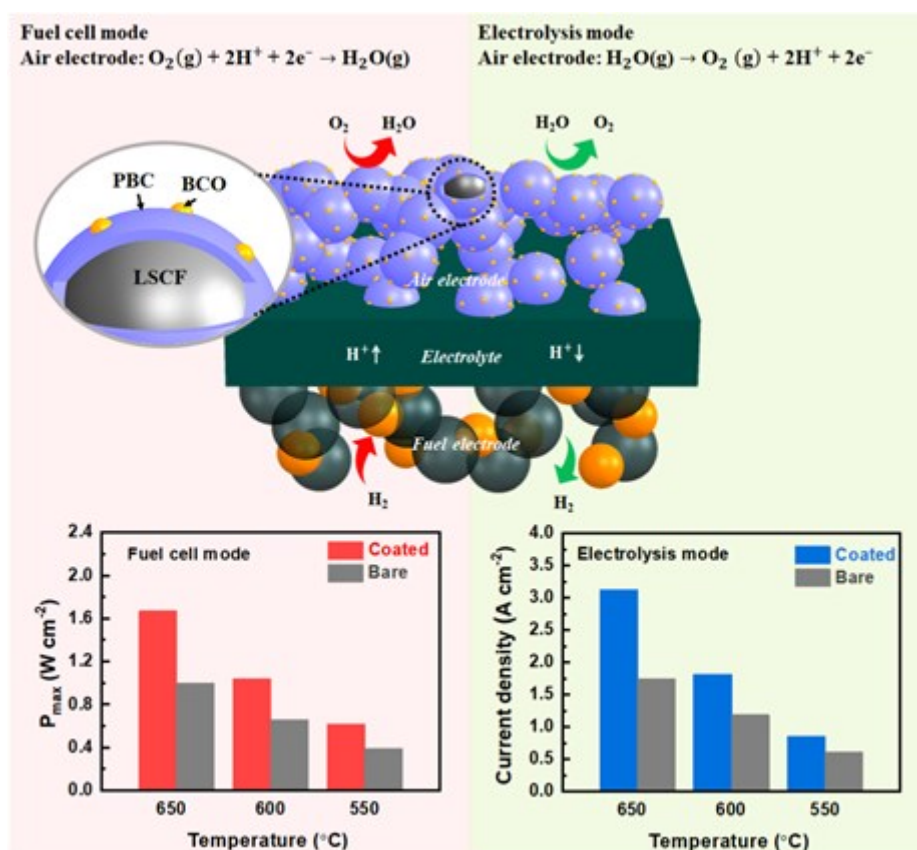
- [43] K. Pei, Y. Zhou, Y. Ding, K. Xu, H. Zhang, W. Yuan, K. Sasaki, Y. Choi, M. Liu, Y. Chen, *Journal of Power Sources* **2021**, 514, 230573.
- [44] W. Gong, M. Yadav, A. J. Jacobson, *MRS Online Proceedings Library* **2009**, 1126, 807.
- [45] Y. Niu, Y. Zhou, W. Lv, Y. Chen, Y. Zhang, W. Zhang, Z. Luo, N. Kane, Y. Ding, L. Soule, Y. Liu, W. He, M. Liu, *Advanced Functional Materials* **2021**, 31, 2100034.
- [46] L. Yang, Z. Liu, S. Wang, Y. Choi, C. Zuo, M. Liu, *Journal of Power Sources* **2010**, 195, 471.
- [47] F. Zhao, C. Jin, C. Yang, S. Wang, F. Chen, *J. Power Sources* **2011**, 196, 688.
- [48] C. Chen, M. Liu, Y. Bai, L. Yang, E. Xie, M. Liu, *Electrochemistry Communications* **2011**, 13, 615.
- [49] S. H. Min, R. H. Song, J. G. Lee, M. G. Park, K. H. Ryu, Y. K. Jeon, Y. g. Shul, *Ceramics International* **2014**, 40, 1513.
- [50] S. Lee, S. Park, S. Wee, H. w. Baek, D. Shin, *Solid State Ionics* **2018**, 320, 347.
- [51] Y. W. Lai, K. R. Lee, S. Y. Yang, C. J. Tseng, S. C. Jang, I. Y. Tsao, S. y. Chen, S. W. Lee, *Ceramics International* **2019**, 45, 22479.
- [52] H. Shimada, Y. Yamaguchi, H. Sumi, Y. Mizutani, *J. Electrochem. Soc.* **2020**, 167, 124506.
- [53] H. Shimada, Y. Yamaguchi, H. Sumi, Y. Mizutanin, *Ceramics International* **2021**, 47, 16358.
- [54] J. H. Kim, S. Yoo, R. Murphy, Y. Chen, Y. Ding, K. Pei, B. Zhao, G. Kim, Y. Choi, M. L. Liu, *Energy & Environmental Science* **2021**, 14, 1506.
- [55] Y. Zhang, Y. Chen, M. Yan, F. Chen, *J. Power Sources* **2015**, 283, 464.
- [56] Y. Zhang, Y. Chen, M. Li, M. Yan, M. Ni, C. Xia, *Journal of Power Sources* **2016**, 308, 1.

A multiphase catalyst-coated LSCF air electrode is developed for reversible protonic ceramic electrochemical cells, demonstrating exceptional activity and excellent stability against H₂O. The high performance of the air electrode is attributed to the high rate of surface oxygen exchange, fast surface proton diffusion, and the rapid H₂O and O₂ dissociation on the catalysts.

Yinghua Niu†, Yucun Zhou†, Weilin Zhang, Yanxiang Zhang, Conor Evans, Zheyu Luo, Nicholas Kane, Yong Ding, Yu Chen, Xuyun Guo, Weiqiang Lv*, Meilin Liu*

Highly Active and Durable Air Electrodes for Reversible Protonic Ceramic Electrochemical Cells Enabled by An Efficient Bifunctional Catalyst

ToC figure



This is the author manuscript accepted for publication and has undergone full peer review but has not been through the copyediting, typesetting, pagination and proofreading process, which may lead to differences between this version and the [Version of Record](https://doi.org/10.1002/aenm.202103783). Please cite this article as [doi: 10.1002/aenm.202103783](https://doi.org/10.1002/aenm.202103783).

This article is protected by copyright. All rights reserved.